# Cross section measurements of the $^{89}Y(p,\gamma)^{90}Zr$ reaction at energies relevant to *p*-process nucleosynthesis

P. Tsagari, M. Kokkoris, E. Skreti, A. G. Karydas, S. Harissopulos,* and T. Paradellis†
*Institute of Nuclear Physics, National Centre for Scientific Research "Demokritos," POB 60228, 153.10 Aghia Paraskevi, Athens, Greece*

P. Demetriou
*Institut d'Astronomie et d'Astrophysique, Université Libre de Bruxelles, Campus de la Plaine, CP 226, 1050 Brussels, Belgium*
(Received 1 December 2003; published 9 July 2004)

In beam angle-integrated cross section measurements of the $^{89}Y(p,\gamma)^{90}Zr$ reaction were carried out at $E_p = 1.7-4.8$ MeV by using a $4\pi$ NaI(Tl) summing detector. The resulting cross sections were used to derive astrophysical *S* factors as well as reaction rates. Cross sections, *S* factors and reaction rates have also been calculated by means of the statistical model code MOST. A good agreement between theoretical predictions and experimental data was found.

DOI: 10.1103/PhysRevC.70.015802 PACS number(s): 25.40.Lw, 24.60.Dr, 26.50.+x, 27.50.+e

## I. INTRODUCTION

The synthesis of the so-called *p* nuclei requires a special mechanism known as *p* process (see, e.g., in [1,2]). This process consists of various nucleosynthetic scenaria in which the formation of the *p* nuclei proceeds mainly by sequences of $(\gamma,n)$, $(\gamma,p)$, and $(\gamma,\alpha)$ reactions. In some of these scenaria certain $(p,\gamma)$ as well as $(\alpha,\gamma)$ reactions could also be involved. The stable *p* nuclei, all 35 of them, are proton-rich nuclei heavier than iron that lie between $^{74}Se$ and $^{196}Hg$, as shown in Fig. 1. They are taken to originate from the "burning" of preexisting, more neutron-rich nuclei at stellar environments of high temperatures ranging from 1.8 to 3.3 billion degrees Kelvin, where all the abovementioned reactions can occur. Such temperature conditions are expected to be fulfilled in, e.g., the O/Ne rich layers of massive stars during their explosion as type II supernovae [3,4]. The production of *p* nuclei via the two known neutron capture nucleosynthetic processes, i.e., the *s* and *r* process [1], is blocked by stable ("seed") nuclei that shield them from the beta decay of more neutron-rich isobars. Consequently, *p* nuclei are typically 10–100 times less abundant than the corresponding more neutron-rich isotopes except for a few cases, the most striking one being that of $^{92}Mo$ with an isotopic abundance of 14.8%.

The prediction of the *p*-nuclei abundances is one of the major puzzles of all models of *p*-process nucleosynthesis. Until now all these models are capable of reproducing these abundances within a factor of 3 (see, e.g., in Refs. [5,6]). However, they all fail in the case of the light *p* nuclei with $A \leqslant 100$. These discrepancies could be attributed to uncertainties in the pure "astrophysical" part of the *p*-process modeling [7,8]. However, they could also result from uncertainties in the nuclear physics input used in the abundance calculations for the following reason: abundance calculations involve an extended network of typically 20 000 nuclear reactions of almost 2000 nuclei with masses ranging from $A = 12$ to 210. The huge number of reaction rates required to solve such a network can hardly be measured in the laboratory. Hence all extended network calculations rely almost entirely on the theoretical rates based on the Hauser-Feshbach (HF) theory [9]. The reliability of the predicted rates can be checked by systematic comparisons with experimental data. A major obstacle, in this respect, is the scant experimental data available in the medium mass region, at astrophysically relevant energies [10–20]. Furthermore, to date, the HF theory has succeeded in reproducing only some of these data. Under these conditions, additional cross section measurements are required in order to extend the systematic comparison between the HF calculations and experiment and thus to gain deeper insight into the uncertainties of the calculations and their origin. For these reasons, we have performed measurements of the cross section of the $^{89}Y(p,\gamma)^{90}Zr$ reaction using, a $4\pi$ summing technique. The results are compared with the predictions of the HF theory obtained with the statistical model code MOST [21]. Different models of nucleon-nucleus optical model potentials (OMPs) and nuclear level densities (NLDs) are considered, in an attempt to evaluate the range of uncertainties they give rise to in the final reaction rates to be used in network calculations.

## II. EXPERIMENTAL SETUP AND PROCEDURES

All measurements were carried out at the 5 MV T11 Van de Graaff Tandem accelerator of the Institute of Nuclear Physics of NCSR "Demokritos" in Athens, Greece. The high voltage of the accelerator was calibrated by means of the 872 keV resonance of the $^{19}F(p,\alpha\gamma)^{16}O$ reaction.

The $^{89}Y(p,\gamma)^{90}Zr$ reaction was studied by varying the proton beam energy from 1.8 to 4.9 MeV. In order to keep the dead time below 5%–7%, especially at $E_p \geqslant 3$ MeV, it was necessary to work with beam currents of less than 300 nA on target. The beam energy spread was $\approx 1.2$ keV at $E_p = 872$ keV. The target used was produced by evaporation of pure (99.99%) metallic $^{89}Y$ on a Ta backing. Directly after

*Corresponding author. Email address: sharisop@inp.demokritos.gr.
†Deceased.

 

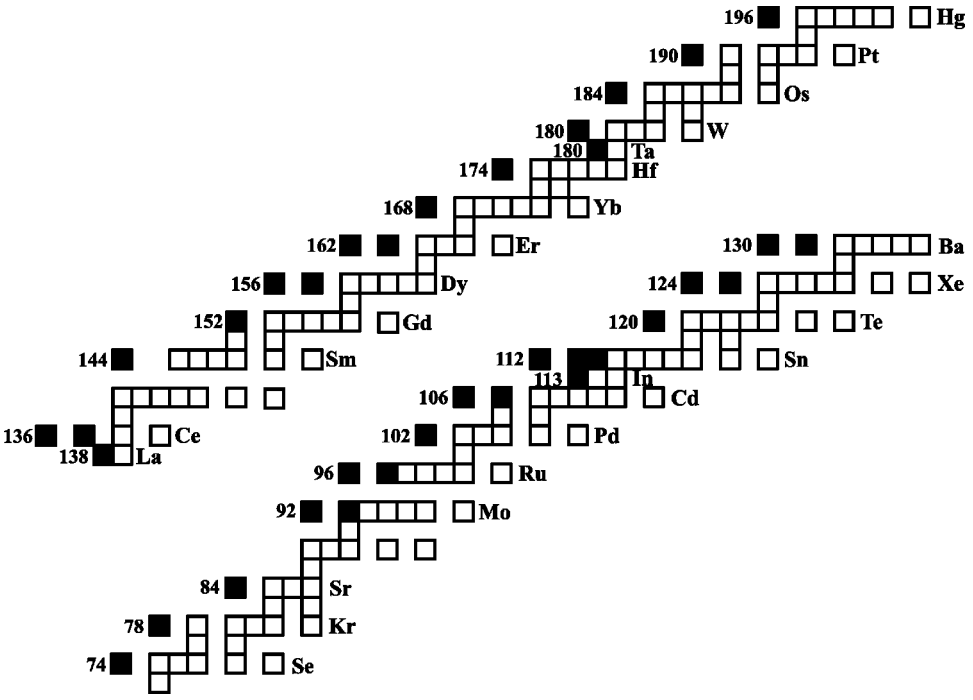


FIG. 1. Chart of the *p* nuclei (black rectangles). Symbols are given only for the elements having *p* isotopes. The numbers displayed indicate the mass number *A* of the lightest *p* isotope of these elements (Ref. [19]).

this procedure, a thin layer of gold of 99.9999% purity was additionally evaporated on the target in order to prevent oxidization. The thickness of the target used was determined by means of the XRF technique, which yielded $436\pm24$ $\mu g/cm^2$ for the $^{89}Y$ layer and $125\pm7$ $\mu g/cm^2$ for the gold "flush." The target was checked for possible deterioration after the end of the measurements and was found to be stable within 2%.

Gamma-single spectra were measured by means of a large 12 in.$\times$12 in. $4\pi$ NaI(Tl) summing detector shown in Fig. 2(a). It has an axial throughhole ($\varnothing=35$ mm) coinciding with the beam axis as well as a radial throughhole ($\varnothing=83$ mm) where two extra 3 in.$\times$3 in. NaI(Tl) detectors were placed, as sketched in Fig. 2(b). The NaI(Tl) detector consists of two scintillation crystals of cylindrical shape with a diameter of 305 mm and a length of 152.5 mm [see Fig. 2(b)]. Each crystal is segmented in four equal parts wrapped with aluminum (0.5 mm thick). With this detector arrangement, a solid angle of $\approx$96% of $4\pi$ is covered for the $\gamma$ rays emitted from the target at the crystals's center. The signals from the photomultipliers were summed, after being first gain matched, and the summed signal was guided to the ADC for data acquisition. The main advantage of using such a $4\pi$ detector is that, instead of measuring and analyzing numerous $\gamma$-cascade transitions, one observes angle-integrated $\gamma$-ray fluxes due to the $4\pi$ geometry covered by the summing crystal; thus, systematic errors due to $\gamma$-angular distribution effects are avoided. As shown in Fig. 2(a), the NaI(Tl) detector is fixed on an iron frame that can be moved on a railway with an accuracy of 0.5 mm, thus ensuring the correct positioning of the target holder at the center of the detector. The detector is surrounded by a 5 cm thick lead "house" (not shown in Fig. 2) that serves as passive shielding against natural radioactivity.

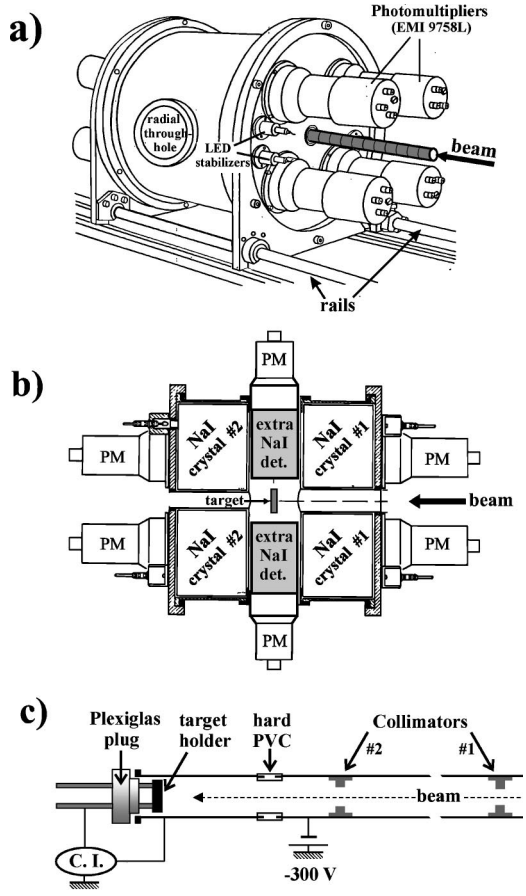


FIG. 2. Sketch of the setup used in the present work: (a) side view of the $4\pi$ NaI(Tl) summing detector; (b) NaI crystal arrangement at the horizontal plane; (c) the beam collimating and target supporting system.

The beam collimating and target supporting system used in the present work is shown in Fig. 2(c). The proton beam passes through two collimators and is focused onto a spot of ≈4 mm diameter on the target. The distance of the target from the first and second collimator was ≈150 and 70 cm, respectively. The first collimator is a Ta plate with a hole of 2 mm diameter whereas the second one is a double collimator consisting of two Ta plates. The first plate has a ∅2 mm hole. The second plate (antiscatterer) has a ∅3 mm hole. The distance between these two plates is 2 cm. The target holder was a hollow copper disk with a diameter of 19 mm. It was placed at the end of a stainless steel tube that was sealed with a plexiglas plug of cylindrical shape. As shown in Fig. 2(c), a PVC cylinder, placed at a distance of 20 cm from the end of the beam tube, was used to isolate the part of the tube that was electrically connected with the target holder. Hence the last part of the beam tube along with the target holder acted as a Faraday cup for current integration. During all measurements a voltage of −300 V was applied in front of the Faraday-cup "entrance," as shown in Fig. 2(c), in order to suppress the secondary electrons escaping from the Faraday cup at steep angles and to prevent the electrons carried by the beam from reaching the target.

The target cooling was achieved indirectly, by cooling the hollow target holder with air flowing into it through two thin copper tubes (∅35 mm) welded on the target holder. These tubes bore through the plexiglas plug to which they are glued with araldite. The use of plexiglas as tube sealing material enables to reduce the absorption of the low energy $\gamma$ rays. A 2 mm thick O ring served as vacuum sealing material between the beam tube and the plexiglas plug. Except for the target holder, the rest of the beam line is sealed with copper gaskets. The beam line includes three cooling traps and four turbopumps, with the last pump located at the beginning of the tube at ≈10 cm distance from the first collimator; thus the carbon buildup on the targets was signifficantly prevented even after severe irradiation. A vacuum of $1 \times 10^{-7}$ mbar was attained with this setup throughout the entire experiment.

The $\gamma$-single spectra measured with the summing detector obviously include not only $\gamma$ rays from the reaction in the target, but also $\gamma$ rays arising from reactions in the Ta backing. Therefore, after measuring spectra produced by the proton beam of a certain energy on the $^{89}$Y target, additional "backing" spectra were taken. This was done by first decreasing the energy of the beam according to the beam energy loss in the gold flush and the $^{89}$Y target and then impinging the beam on a blank Ta backing. The latter "backing" spectra were subsequently subtracted from the former ones after first being normalized to the same charge. The resulting *difference* spectra are expected to be free from $\gamma$ peaks arising from reactions occurring in the Ta backing. This, however, was not the case for the $\gamma$ transitions arising from the contaminant $^{19}\mathrm{F}(p,\alpha\gamma)^{16}\mathrm{O}$ reaction, which at low energies excites broad resonances and therefore increases (see, e.g., [22]). In order to overcome this problem and avoid systematic errors in our analysis, only $\gamma$-ray fluxes with photon energies above 8 MeV were used to determine the cross section of the reaction of interest, as described in the Sec. III. A typical example of $\gamma$-single spectra measured as described above, is shown in Fig. 3 for $\gamma$ rays with energies $E \geqslant 2.8$ MeV.

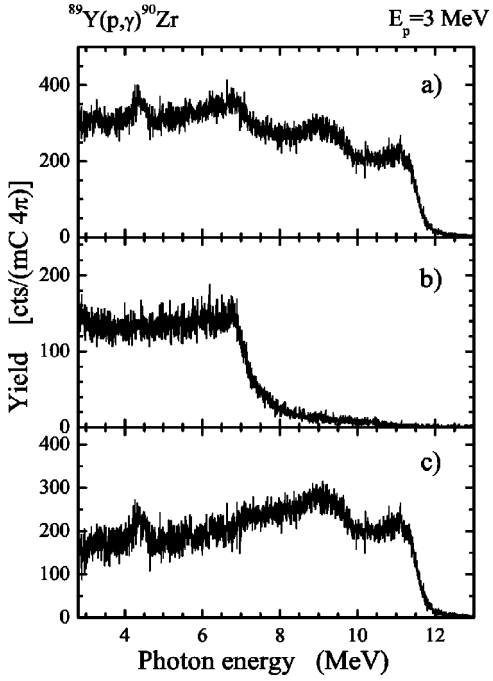


FIG. 3. Gamma-single spectra measured at $E_p = 3$ MeV by (a) impinging the beam on the target, and (b) impinging the beam on the Ta backing after decreasing properly the beam energy. The spectrum shown in (c) is the "difference" spectrum resulting from the subtraction of spectrum shown in (b) from that plotted in (a). The results of the present work have been derived from the analysis of difference spectra. The peak at ≈4.24 MeV is to be attributed to the decay of the $2_2^+$ state of the $^{24}$Mg nucleus that is produced by the $^{23}\mathrm{Na}(p,\gamma)^{24}\mathrm{Mg}$ reaction occurring most probably due to the presence of small amounts of Na in the target material.

## III. DATA ANALYSIS AND RESULTS

In order to obtain the total cross section $\sigma_T$, the absolute yield $Y_0$, i.e., the absolute number of all photons emmitted by the $^{89}\mathrm{Y}(p,\gamma)^{90}\mathrm{Zr}$ reaction, has to be determined. The absolute yield $Y_0$ is given by

$$Y_0 = \frac{F}{Q}\frac{1}{\epsilon}, \tag{1}$$

where $F$ is the angle-integrated $\gamma$-ray flux measured at energy $E$, $Q$ is the corresponding accumulated charge and $\epsilon$ is the absolute efficiency of the detector. The experimental yields $Y_{\mathrm{exp}} = F/Q$ were obtained from the "difference" spectra described in Sec. II, whereas the absolute efficiency $\epsilon$ was obtained from Monte Carlo simulations described in the following.

The absolute efficiency $\epsilon$ of the summing detector has been determined in the past [22] with radioactive sources as well as by means of the reactions $^{19}\mathrm{F}(p,\alpha\gamma)^{16}\mathrm{O}$ and $^{9}\mathrm{Be}(p,\gamma)^{10}\mathrm{B}$. These reactions provide $\gamma$ rays of up to 7.6 MeV, with very well known intensities, from resonances that have been extensively investigated. $\epsilon$ was additionally

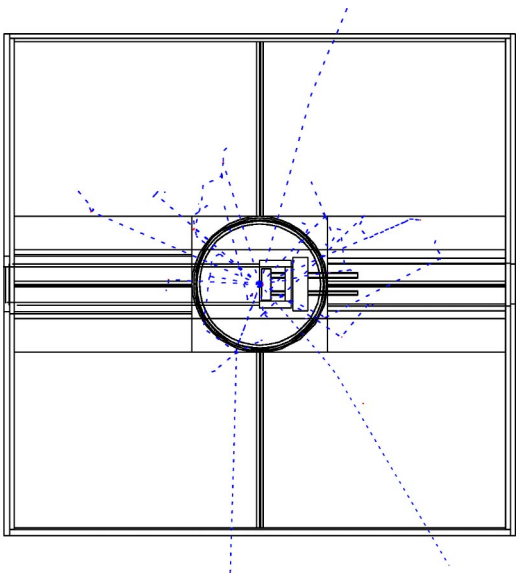

FIG. 4. (Color online): side view of the GEANT-simulated geometry of the experimental setup. Dashed lines indicate simulated "paths" of $\gamma$ rays emmitted from the center of the target.

determined by Monte Carlo simulations in [22] and was found to agree within 6%–8% with the experimental ones. However, although in Ref. [22] all resonances used to determine $\epsilon$ resulted in $\gamma$ cascades with multiplicity $M \leqslant 2$, in the present case $\gamma$ cascades with $M > 2$ could not be excluded *à priori*. Furthermore, there are substantial differences between the target holder of [22] and the one used in the present work. For these reasons, new Monte Carlo simulations had to be performed to determine the absolute efficiency $\epsilon$ of the summing detector using the code GEANT [23].

The first step in our simulations was to describe the experimental setup properly, i.e., the geometry as well as the materials from which all the setup components are made. For this purpose, 75 independent volumes of various shapes and different materials were taken into account in order to simulate the target, the holder, the beam tube, and the detector itself. The resulting geometry is shown in Fig. 4.

The next step in the simulation procedure was to define the energies of the $\gamma$ transitions depopulating the excited states of the produced $^{90}$Zr nucleus, as well as the multiplicities of the involved $\gamma$ cascades. This task required the knowledge of the level scheme of $^{90}$Zr up to an excitation energy of $E_X = Q + E_{\mathrm{c.m.}}$, where $Q$ is the $Q$ value of the reaction, $E_{\mathrm{c.m.}}$ is the beam energy in the center-of-mass system and $E_X$ is the excitation energy of the entry state populated in the compound nucleus. In our case, the beam energy varied from 1.7 to 4.8 MeV and the $Q$ value of the $^{89}\mathrm{Y}(p,\gamma)^{90}\mathrm{Zr}$ reaction is 8.35 MeV. The resulting relevant level scheme was rather complicated since $E_X$ was large with values ranging from $\approx 10$ to $\approx 13.1$ MeV.

At first, we constructed a level scheme according to the known excited states of $^{90}$Zr given in the compilation of Firestone *et al.* [24]. The level scheme was complicated and the number of the cascading $\gamma$ transitions was large ($\geqslant 40$). As a result, the simulation procedure was rather involved and led to ambiguous results. To overcome these problems, we considered not only one, unique level scheme to describe the decay pattern of $^{90}$Zr, but different ones depending on the beam energy. All the different level schemes that were assumed had one thing in common: the first excited state was the $2_1^+$ state at 2186 keV excitation energy given by [24]. Otherwise, $N$ additional higher lying states were taken to exist every 500 keV, starting from the respective entry state down to the the $2_1^+$ state.

The level schemes constructed as descibed above included many $\gamma$ cascades of various multiplicities $M$. In particular, we took into account: (a) the $\gamma$ ray from the entry state to the ground state ($\gamma_0$ transition), (b) a twofold $\gamma$ cascade consisting of the primary $\gamma$ transition from the entry state to the $2_1^+$ state ($\gamma_1$ transition) and the 2186 keV $\gamma$ transition from the $2_1^+$ state to the ground state, and (c) three- and fourfold $\gamma$ cascades. In any three- and fourfold cascade, the initial cascading transition was always the $\gamma$ ray deexciting the entry state and the final one was the 2186 keV $\gamma$ transition from the $2_1^+$ state to the ground state. It has to be noted that, due to the assumption that the excited states are equally spaced (500 keV), some of the three- and fourfold cascades were formed by $\gamma$ transitions of the same energy but of difference sequence. These cascades were taken into account only once since it is the energy and not the sequence of the cascading transitions that is relevant for the simulations. Finally, $\gamma$ cascades with $M > 4$ were not taken into account since the best agreement with the spectra was obtained with the simulations assuming $M \leqslant 4$. Furthermore, there was no significant improvement in the reproduction of the measured difference spectra by including $\gamma$ cascades with $M > 4$. A typical example of a level scheme constructed with the above criteria is shown in Fig. 5. It was adopted in the simulations of the "difference" spectra measured at $E_p = 3$ MeV. As shown in the figure, the adopted level scheme includes 16 different excited levels and the ground state. Because of the adopted counting criteria, some of the levels fulfilling the 500 keV spacing criterion, like, e.g., those at 7321 or at 9821 keV, are omitted from the level scheme in Fig. 5.

The decay of the excited $^{90}$Zr nuclei produced at $E_p = 3$ MeV is described by 16 decay "modes" shown in Fig. 5, i.e., the $\gamma_0$ transition (onefold), the twofold $\gamma$ cascade ($E_X \rightarrow 2186$, and $2186 \rightarrow 0$), plus ten different three and four different fourfold $\gamma$ cascades. In our simulations, every decay "mode" was simulated independently with $10^5$ photons, i.e., 16 different GEANT runs were performed.

The input data in each GEANT run consisted of two sets of information: (a) the geometry of the setup components with their composition (atomic number, density, etc.) that was the same in every run and (b) the number and energies of the photons to be simulated. As mentioned above, the number of photons was $10^5$, whereas the energies varied according to the 16 different decay "modes." The output of each GEANT simulation was a histogram showing the number of the photons with respect to the energy deposited in the crystal. The ten histograms resulting from the simulations of the different threefold cascades were summed. The same was done for the case of the fourfold cascades. In this way, four different histograms were obtained corresponding to the four different multiplicities assumed to describe the decay of the excited $^{90}$Zr nuclei ($\gamma_0$ transition, two-, three-, and fourfold $\gamma$ cas-

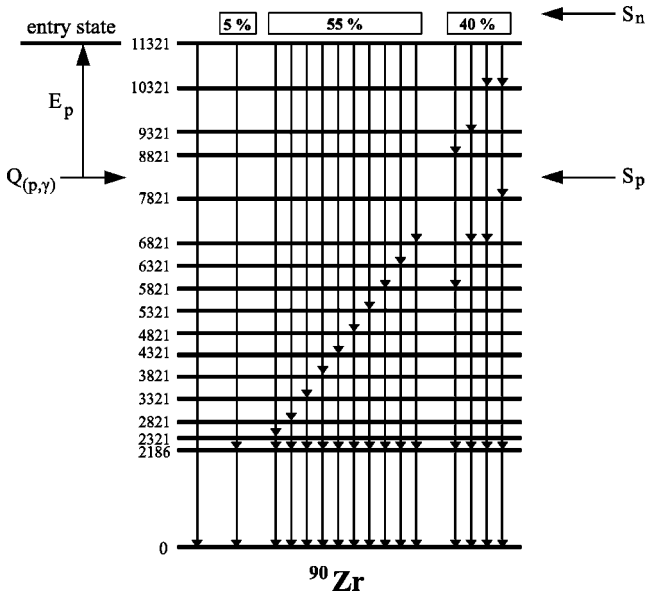


FIG. 5. Level scheme of $^{90}$Zr assumed in the present work to perform the Monte Carlo simulations at $E_p$=3 MeV. The proton ($S_p$) and neutron ($S_n$) separation energies of $^{90}$Zr are indicated with arrows on the right side. The $Q$ value of the reaction in consideration as well as the "entry state" of the $^{90}$Zr nucleus produced at $E_p$=3 MeV are shown on the left side. Numbers in % given at the top of the level scheme indicate the relative yield contribution of the corresponding type of $\gamma$ cascade that were derived from the simulations.

cades). For the needs of the analysis, all the histograms were "normalized" to the same number ($10^5$) of simulated photons, i.e., the content of each bin of the summed histograms of the three- and fourfold cascades were divided by a factor of 10 and 4, respectively. All four histograms were then convoluted with a Gaussian response function in order to take into account the resolution of the summing detector at different energies. The resulting spectrum was subsequently matched to the energy calibration of the ADC used in the acquisition of the data. The Gaussian response function was determined from the analysis of $\gamma$ rays of spectra of radioactive sources ($^{137}$Cs, $^{60}$Co) as well as spectra measured at the 872 and 989 keV resonances of the $^{19}$F$(p,\alpha\gamma)^{16}$O and the $^{9}$Be$(p,\gamma)^{10}$B reaction, respectively.

In order to determine the absolute efficiency $\epsilon$ of the detector, a $\chi^2$ fit was first used to minimize the quantity $Y_{\mathrm{sim}}$ given by

$$Y_{\mathrm{sim}} = Y_{\mathrm{exp}} - (b_1F_1 + b_2F_2 + b_3F_3 + b_4F_4), \tag{2}$$

where $Y_{\mathrm{exp}}$ is the experimental yield obtained by integrating the "difference" spectrum measured at an energy $E_p$, $F_1$, $F_2$, $F_3$, $F_4$ are the integrals of the convoluted spectra obtained from *GEANT* for the one-, two-, three-, and fourfold cascades at this energy, respectively, and $b_1$, $b_2$, $b_3$, and $b_4$ are weighting factors obtained from the fitting procedure. These factors represent the relative yield contributions of the corresponding types of $\gamma$ cascade and are constrained by the relation

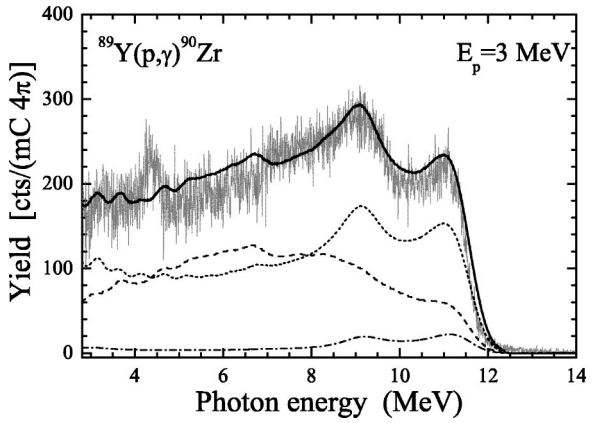


FIG. 6. Experimental and simulated $\gamma$ spectra at $E_p$=3 MeV. The dotted and dashed curves indicate the simulated $\gamma$ flux due to four- and threefold cascades, respectively. The dashed-dotted curve correspond to the simulated yield of the twofold cascades. The contribution of the $\gamma_0$ transition (onefold) to the plotted yield is not shown since it is negligible. The solid curve is the sum of the latter three simulated spectra. The agreement with the experimental $\gamma$ spectrum shown as grey histogram is very good.

$$\sum_{j=1}^{4} b_j = 1. \tag{3}$$

The $b_j$ factors obtained from the above fitting procedure were finally used to evaluate the absolute efficiency $\epsilon$ by

$$\epsilon = \frac{b_1F_1 + b_2F_2 + b_3F_3 + b_4F_4}{N_T}, \tag{4}$$

where $N_T$ is the total number of the simulated photons, i.e., $4\times10^5$.

A typical example of the agreement between the experimental and simulated spectra at $E_p$=3 MeV is given in Fig. 6. The simulation of the spectra shows that the yield contribution of the $\gamma_0$ transition (onefold cascade) is negligible, i.e., below 0.5%, at all the measured energies. Moreover, the yield of the fourfold cascades, i.e., the weighting factor $b_4$ increases with increasing beam energy in contrast to the respective yield of the three- and twofold cascades that decreases. This is illustrated in Fig. 7, where the factors $b_2$, $b_3$, and $b_4$ are plotted with respect to beam energies measured in the present work. This effect is somehow expected, since an increase in the beam energy results in an increase in the excitation energy $E_X$ of the produced nuclei, and hence the probabillity of having high-fold $\gamma$ cascades increases as well. This could obviously affect the efficiency of the summing detector.

The absolute efficiencies $\epsilon$ obtained by the simulation procedure described above for the energy regions 2.8–14 and 8–14 MeV are shown in Fig. 8. Due to the problems arising from the $^{19}$F$(p,\alpha\gamma)^{16}$O reaction discussed in Sec. II, the $\gamma$-ray fluxes up to $\approx$7.3 MeV could include events from this contaminant reaction. As a consequence, only the experimental fluxes $F$ in the 8–14 MeV region and the corresponding

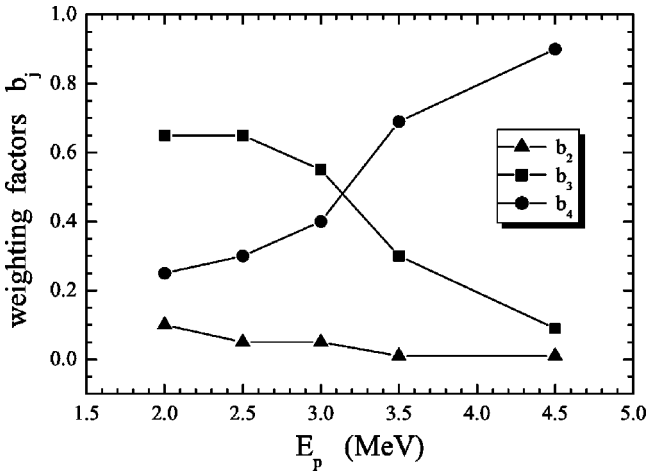


FIG. 7. Weighting factors $b$ resulted from the simulations vs some measured beam energies. $b_2$, $b_3$, and $b_4$ correspond to the relative yield contribution of the two-, three, and fourfold $\gamma$ cascades, respectively.

absolute efficiencies $\epsilon$ have been used to obtain the absolute yields $Y_0$ defined in Eq. (1). The total cross section $\sigma_T$ was then obtained from

$$\sigma_T = Y_0 \frac{A}{N_A} \frac{1}{\xi}, \tag{5}$$

where $A$ is the atomic weight of the target in amu, $N_A$ is the Avogadro number, and $\xi$ is the target thickness. The resulting total cross sections $\sigma_T$ at the center-of-mass energy as well as the corresponding astrophysical $S$-factors are given in Table I. The energies given in the first column of Table I are the effective energies $E_{\text{eff}}$ in the center-of-mass system. They were determined by using appropriate stopping powers [25] by

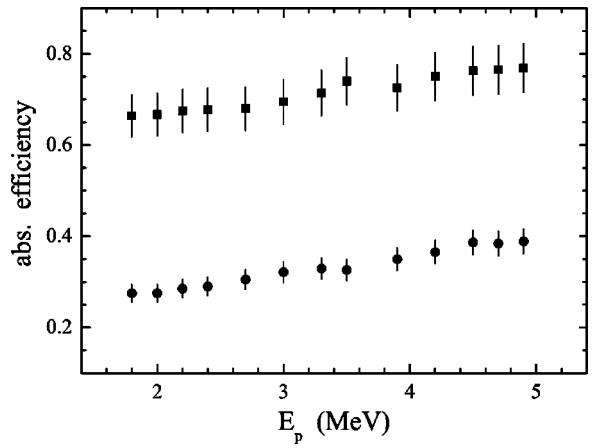


FIG. 8. Absolute efficiency vs beam energy determined in the present work: rectangles correspond to the efficiencies obtained by integrating the $\gamma$ flux from 2.8 to 14 MeV, whereas circles are those derived for the 8–14 MeV region. The indicated errors range from 6% to 9% of the corresponding value.

TABLE I. Total cross sections ($\sigma_T$) and astrophysical $S$ factors ($S$) of the $^{89}\text{Y}(p,\gamma)^{90}\text{Zr}$ reaction determined in the present work. $E_{\text{c.m.}}$ is the center-of-mass energy.

| $E_{\text{c.m.}}$ (MeV) | $\sigma_T(\mu\text{b})$ | $S$ ($10^7$ keV*b) |
|---|---|---|
| 1.757 | 8±2 | 5816±1454 |
| 1.961 | 26±5 | 4466±859 |
| 2.160 | 40±6 | 2068±310 |
| 2.359 | 118±16 | 2154±292 |
| 2.656 | 339±42 | 1645±204 |
| 2.953 | 704±86 | 1122±137 |
| 3.250 | 1351±150 | 830±92 |
| 3.448 | 1903±210 | 665±73 |
| 3.843 | 2690±296 | 351±39 |
| 4.140 | 2936±294 | 202±20 |
| 4.437 | 2281±230 | 88±9 |
| 4.635 | 2127±192 | 58±5 |
| 4.832 | 2152±194 | 42±4 |

$$E_{\text{eff}} = E_p - \Delta E_{\text{Au}} - \frac{\Delta E_Y}{2}, \tag{6}$$

and were subsequently transformed to the center-of-mass system. In the latter equation, $E_p$ is the beam energy. $\Delta E_{\text{Au}}$ and $\Delta E_{\text{Y}}$ are the energy losses in the gold layer and the target material, respectively.

The astrophysical $S$ factors given in Table I are given by

$$S(E) = \sigma_T(E) E e^{2\pi\eta}, \tag{7}$$

where $\eta$ is the Sommerfeld parameter [26] defined by

$$2\pi\eta = 31.29 Z_1 Z_2 \left(\frac{\mu}{E}\right)^{1/2}. \tag{8}$$

In the last equation, the reduced mass $\mu$ is in amu and the center-of-mass energy $E$ is in units of keV so that the $S$ factors are in keV $b$.

The total errors in the cross sections given in Table I are of the order of 9%–12% except for those in the cross sections determined at the four lowest energies. The latter errors range from 15% to 25%. Apart from statistical errors of $\leqslant 3\%$ at $E_p \geqslant 2.5$ MeV and $\approx 10\% - 15\%$ at $E_p < 2.5$ MeV, we also took into account errors of 5%, and 4% due to charge and target thickness measurements, respectively. An additional 6%–9% error in the simulated efficiency was also taken into account.

## IV. DISCUSSION

The main goal of the present work is, apart from contributing to cross section systematics necessary for astrophysical applications, to investigate the validity of the different nuclear ingredients of the HF calculations. In the HF theory [9], the cross section for the decay of a compound nucleus into one of the exit channels is given by

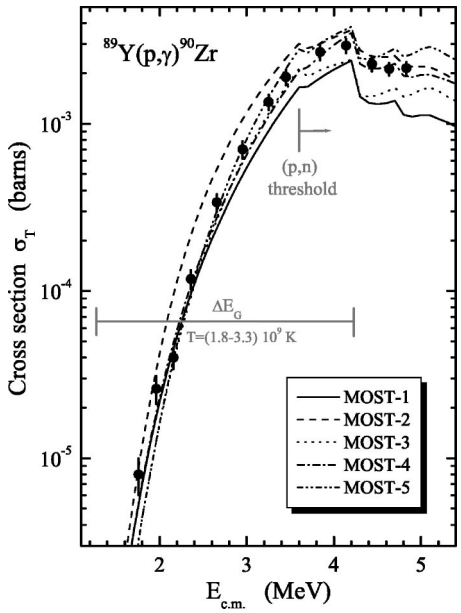


FIG. 9. Comparison of the cross sections (solid circles) measured in the present work with the predictions of the HF theory (curves) calculated with the code MOST. The different curves correspond to the different combinations of OMPs and NLDs used in the calculations. The solid, dashed and dotted curves result from the combination of the microscopic NLD of Demetriou and Goriely (Ref. [38]) with the OMPs of Jeukenne *et al.* [35] (MOST-1), Bauge *et al.* [36] (MOST-2), and Koning and Delaroche [34] (MOST-3), respectively. The dot-dashed and the dot-dot-dashed curves have been obtained from the combination of the macroscopic NLD of Thielemann *et al.* [37] with the OMPs of Jeukenne *et al.* [35] (MOST-4), and Koning and Delaroche [34] (MOST-5), respectively. The Gamow window $\Delta E_G$ corresponding to the stellar temperatures $T=(1.8-3.3)\times 10^9$ K that are relevant to the *p* process is indicated with the horizontal line.

$$\sigma_{\alpha\beta} = \pi\lambda_\alpha^2 \frac{1}{(2I+1)(2i+1)} \sum_{J^\pi} (2J+1) \frac{T_\alpha^{J^\pi} T_\beta^{J^\pi}}{\sum_{\alpha'} T_{\alpha'}^{J^\pi}}, \qquad (9)$$

where $\alpha$, $\beta$ denote the entrance and exit channels respectively, and $I$, $i$ are the target and projectile spins respectively. $T_{\alpha,\beta}^{J^\pi}$ are the transmission coefficients summed over all orbital and channel spins to give the total transmission coefficient for the formation of the compound nucleus in the state $J^\pi$. When the compound nucleus is excited to states in the continuum, the transmission coefficients in Eq. (9) are averaged over a specified nuclear level density.

Therefore, apart from the *Q* values of the decay channels, the other main nuclear properties the HF cross section depends on are the transmission coefficients for particle and photon emission, and the nuclear level densities of the compound and residual nuclei in the different decay channels. For the sake of nucleosynthesis applications, one needs to develop global models that would enable the evaluation of these properties for the thousands of nuclei and nuclear reactions involved, in a most reliable way. For this purpose, there exist global phenomenological models of nuclear level densities, based on the Fermi gas model description of the excited nucleus, and also microscopic models based on single-particle spectra associated with realistic effective potentials. The main advantage of the latter models is that they take into account the discrete structure of the nucleus and treat shell, pairing and deformation effects consistently, whereas the former models consider these effects by means of empirical corrections. For the transmission coefficients for particle emission there exist purely phenomenological global optical model potentials and microscopic ones. The latter are obtained from nuclear matter calculations using realistic effective interactions. For photon emission, assuming that dipole transitions dominate in the $\gamma$ emission channel, the electric- and magnetic-dipole (GDR) strength functions are commonly described by Lorentz-type functions. The GDR energies and widths are obtained from experimental data

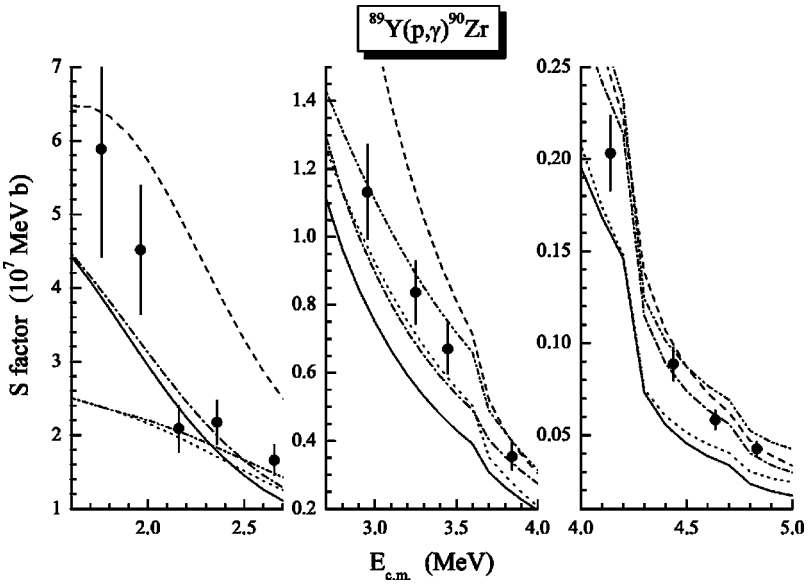


FIG. 10. Plot of the *S* factors (solid circles) resulting from the cross sections measured in the present work. The different curves are the *S* factors obtained from the HF cross-section predictions shown in Fig. 9. The type of the curves in Fig. 10 corresponds to the same type of the curves plotted in Fig. 9 depending to the combination of OMP and NLD used in the cross-section calculations.

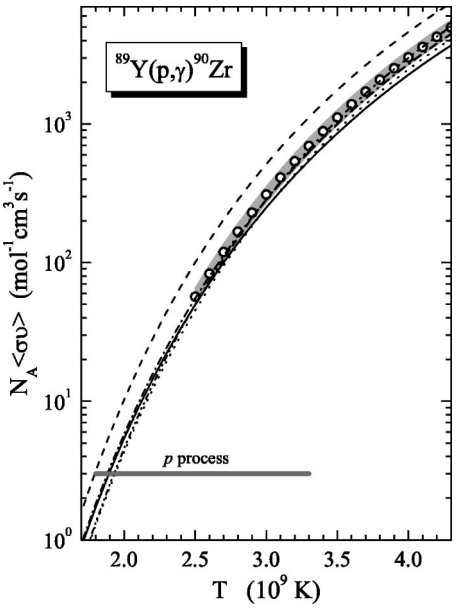


FIG. 11. Ground-state rates of the $^{89}$Y$(p,\gamma)^{90}$Zr reaction vs temperature. Rates obtained from the data are shown as open circles. The experimental uncertainties are depicted by the shaded area. The reaction rates calculated from the cross sections obtained by the statistical model code MOST are shown by curves. The different types of curves correspond to the different combinations of OMP and NLD used in the cross-section calculations similarly to those curves that are plotted in Figs. 9 and 10. The temperature range relevant to the *p* process are indicated by the horizontal bar.

where they exist, otherwise they are determined by appropriate global parametrizations. Recently, microscopic calculations of the GDR strength functions have also been performed using a Hartree-Fock-QRPA model [27].

In the present work, the calculations of the HF cross sections are carried out with the statistical model code MOST [21]. All available experimental data on nuclear masses, deformation, spectra of low-lying states, and GDR energies and widths are taken into account. The nuclear masses are taken from the compilation of Audi and Wapstra [28] and the ground state properties (matter density, single-particle level scheme) are predicted by the microscopic Hartree-Fock-BCS model of [29]. At the low incident energies studied in the current experiment, the most dominant decay channels are those of photon and neutron emission. The alpha-particle emission channel becomes important at energies above $\approx$7 MeV. On the other hand, the effect of using different Lorentz-type or microscopic strength functions for the photon transmission coefficient turns out to be negligible. Therefore, in the following calculations we adopt the alpha-nucleus potential of Demetriou *et al.* [30] and the $E1$ strength functions given by the hybrid model of Goriely [31]. The $M1$ strength functions are parametrized according to [32], with the energies and widths chosen according to the latest recommendations of [33]. While the HF cross sections do not seem to be sensitive to the abovementioned nuclear ingredients, they show a strong dependence on the NLDs and nucleon OMPs. We therefore, use different combinations of NLDs and OMPs in order to investigate the range of uncertainties they give rise to in the predictions of cross sections, *S* factors, and ground-state reaction rates.

In particular, we use the OMPs of (a) Koning and Delaroche [34], (b) Jeukenne *et al.* [35], and (c) Bauge *et al.* [36] The first potential is purely phenomenological whereas the last two are based on microscopic infinite nuclear matter calculations applied with the local density approximation. We adopt two NLD formulas, namely the purely macroscopic densities of Thielemann *et al.* [37] and the statistical microscopic ones of Demetriou and Goriely [38]. The latter NLDs have been readjusted to reproduce the existing data on low-lying excited states and *s*-wave neutron resonance spacings.

Five different combinations of these OMPs and NLDs have been considered in the calculations and the resulting cross sections are compared with the experimental data in Fig. 9. The solid, dashed, and dotted curves correspond to the same microscopic NLDs, namely those of Demetriou and Goriely [38], and the OMPs of Jeukenne *et al.* [35], Bauge *et al.* [36], and Koning and Delaroche [34], respectively. The dot-dashed and dot-dot-dashed curves are obtained from the combinations of the macroscopic NLD of Thielemann *et al.* [37] with the microscopic OMP of Jeukenne *et al.* [35] and the phenomenological OMP of Koning and Delaroche [34], respectively.

The corresponding predictions for the *S* factor are compared with the experimental ones in Fig. 10. The latter figure allows for a more transparent and detailed comparison between theory and experiment since the *S* factors have a smoother variation with energy than the cross sections.

According to Fig. 10, the *S* factors calculated with the OMP of Koning and Delaroche [34] (dotted and dot-dot-dashed curves), show a rather flat energy dependence and fail to reproduce the lowest two experimental data points. The results of the combination of the OMP of Bauge *et al.* [36] with the NLDs of Demetriou and Goriely [38] both microscopic models, overestimate the *S* factors at energies below $\approx$3.5 MeV, by a factor $\approx$2. On the other hand, the other microscopic set, namely that of the OMP of Jeukenne *et al.* [35] and the NLDs of Demetriou and Goriely [38] underestimates the data over the whole energy range, by a factor of $\approx$1.2. Overall, in the energy region covered by the measurements, the *S* factors seem to be more sensitive to the OMPs than the NLDs, particularly in the low energy region. With increasing energy the different NLDs also seem to have an impact, and differences show up in the *S* factors. This can be seen by comparing, e.g., the solid and the dot-dashed curves resulting from the same OMP, i.e., that of [35] and the NLDs of [38] and [37], respectively. The same observation holds for the dotted and dot-dot-dashed curves, obtained from the OMP of [34] combined with the NLDs of [38,37], respectively.

In order to investigate the potential impact of the above-observed uncertainties in nucleosynthesis calculations, it is necessary to compare the corresponding reaction rates calculated at the relevant stellar temperatures. The ground-state rates were obtained from the respective cross sections $\sigma(E)$ by means of

$$\langle \sigma v \rangle = \left( \frac{8}{\pi \mu} \right)^{1/2} \frac{1}{(kT)^{3/2}} \int_0^\infty \sigma(E) \cdot E \cdot \exp\left( - \frac{E}{kT} \right) dE, \tag{10}$$

where $\mu$ is the reduced mass, $kT$ is the thermal energy, and $E$ is the center-of-mass energy. The results are shown in Fig. 11, where the different curves correspond to the same combinations of NLDs and OMPs as in Figs. 9 and 10. The shaded area depicts the range of the uncertainties resulting from the experimental errors in the cross sections.

It is clear that the theoretical reaction rates resulting from the five different combinations of NLDs and OMPs, agree with those obtained from experiment within a $2\sigma$ factor, with the exception of the rates obtained from the OMP of Bauge *et al.* [36] (dashed curve). However, even in this case, the observed discrepancies are within a factor of 2.

## V. CONCLUSIONS

The cross section of the $^{89}$Y$(p,\gamma)^{90}$Zr reaction was measured at $E_P = 1.7-4.8$ MeV and was found to range from $\approx 6$ $\mu b$ to 2.2 mb with relative errors decreasing from 25 down to 9% with increasing beam energy. The data as well as the resulting $S$ factors were compared with the predictions of the statistical model code MOST [21].

Five different combinations of microscopic, as well as phenomenological, OMPs and NLDs were considered in the HF calculations. Among the different OMPs used, the microscopic one of Jeukenne *et al.* [35] seems to give the best overall description of the data, especially when combined with the macroscopic level densities of Thielemann *et al.* [37]. The phenomenological OMP of Koning and Delaroche [34] shows a smoother energy dependence compared to the experimental data. Finally, the OMP of Bauge *et al.* [36] overestimates the data at energies below $\approx 3.5$ MeV. Apart from the latter case, all the other combinations adopted herein, are able, on the whole, to give a satisfactory reproduction of the data with an uncertaintiy of $\approx 20\%$. These uncertainties reflect our limited knowledge of the nuclear level densities and the nucleon-nucleus potentials at low energies of astrophysical relevance.

Nevertheless, by comparing the resulting reaction rates one may conclude that for the specific reaction studied herein, the HF theory agrees with the experiment within a factor of less than 2. Uncertainties of this magnitude in the nuclear physics input in nucleosynthesis calculations, can be considered of minor importance compared to the huge uncertainties (often exceeding orders of magnitudes) involved in the "pure astrophysical" modeling. Our findings however have to be further confirmed by studying an extensive data base of cross sections covering a broad mass range at astrophysically relevant energies.

## ACKNOWLEDGMENT

P.D. acknowledges support through a European "Marie Curie" grant at ULB.

[1] G. Wallerstein *et al.*, Rev. Mod. Phys. **69**, 995 (1997).
[2] M. Arnould and S. Goriely, Phys. Rep. **384**, 1 (2003).
[3] M. Rayet, M. Arnould, M. Hashimoto, N. Prantzos, and K. Nomoto, Astron. Astrophys. **298**, 517 (1995).
[4] S. E. Woosley and W. M. Howard, Astrophys. J., Suppl. **36**, 285 (1978).
[5] M. Rayet, N. Prantzos, and M. Arnould, in *Origin and Distribution of the Elements*, edited by G. Mathews (World Scientific, Singapore, 1987), p. 625.
[6] T. Rauscher, A. Heger, R. D. Hoffman, and S. E. Woosley, Astrophys. J. **576**, 323 (2002).
[7] V. Costa, M. Rayet, R. A. Zappalà, and M. Arnould, Astron. Astrophys. **358**, L67 (2000).
[8] S. M. Asida and D. Arnett, Astrophys. J. **545**, 435 (2000).
[9] W. Hauser and H. Feshbach, Phys. Rev. **87**, 366 (1952).
[10] C. E. Laird, D. Flynn, R. L. Hershberger, and F. Gabbard, Phys. Rev. C **35**, 1265 (1987).
[11] T. Sauter and F. Käppeler, Phys. Rev. C **55**, 3127 (1997).
[12] J. Bork, H. Schatz, F. Käppeler, and T. Rauscher, Phys. Rev. C **58**, 524 (1998).
[13] F. R. Chloupek, A. StJ. Murphy, R. N. Boyd, A. L. Cole, J. Görres, R. T. Guray, G. Raimann, J. J. Zach, T. Rauscher, J. V. Schwarzenberg, P. Tischhauser, and M. C. Wiescher, Nucl. Phys. **A652**, 391 (1999).
[14] S. Harissopulos, E. Skreti, P. Tsagari, G. Souliotis, P. Demetriou, T. Paradellis, J. W. Hammer, R. Kunz, C. Angulo, S. Goriely, and T. Rauscher, Phys. Rev. C **64**, 055804 (2001).
[15] S. Harissopulos, S. Galanopoulos, P. Tsagari, P. Demetriou, G. Kuburas, T. Paradellis, R. Kunz, J. W. Hammer, R. Kunz, G. Gyürky, E. Somorjai, S. Goriely, S. Kasemann, A. Dewald, and K. O. Zell, Nucl. Phys. **A688**, 421 (2001).
[16] G. Gyürky, E. Somorjai, Zs. Fülop, S. Harissopulos, P. Demetriou, and T. Rauscher, Phys. Rev. C **64**, 065803 (2001).
[17] G. Gyürky, E. Somorjai, T. Rauscher, and S. Harissopulos, Nucl. Phys. **A688**, 90 (2001).
[18] N. Özkan, A. StJ. Murphy, R. N. Boyd, A. L. Cole, R. deHaan, M. Famiano, J. Göerres, R. T. Güray, M. Howard, L. Sahin, and M. C. Wiescher, Nucl. Phys. **A688**, 459 (2001).
[19] S. Galanopoulos, P. Demetriou, M. Kokkoris, S. Harissopulos, R. Kunz, M. Fey, J. W. Hammer, Gy. Gyürky, Zs. Fülop, E. Somorjai, and S. Goriely, Phys. Rev. C **67**, 015801 (2003).
[20] G. Gyürky, Zs. Fülöp, E. Somorjai, M. Kokkoris, S. Galanopoulos, P. Demetriou, S. Harissopulos, T. Rauscher, and S. Goriely, Phys. Rev. C **68**, 055803 (2003).
[21] S. Goriely, in *Nuclei in the Cosmos V*, edited by N. Prantzos and S. Harissopulos (Edition Frontières, Paris, 1998), p. 314, see also http://www-astro.ulb.ac.be.
[22] K. Spyrou, C. Chronidou, S. Harissopulos, S. Kossionides, and T. Paradellis, Z. Phys. A: Hadrons Nucl. **357**, 283 (1997).
[23] Code GEANT—Detector Description and Simulation Tool, CERN, Geneva 1993 (unpublished), see also http://wwwasdoc.web.cern.ch/wwwasdoc/geant_html3/geantall.html.

[24] R. B. Firestone, V. S. Shirley, C. M. Baglin, J. Zipkin, and S. Y. F. Chu, *Table of Isotopes*, 8th ed. (Wiley-Interscience, New York, 1996).
[25] J. F. Ziegler and J. P. Biersack, code SRIM, version 2000.39. Full description given by J. F. Ziegler, J. P. Biersack, and U. Littmark, *The Stopping and Range of Ions in Solids* (Pergamon, New York, 1985).
[26] C. E. Rolfs and W. S. Rodney, *Cauldrons in the Cosmos* (The University of Chicago Press, Chicago, 1988), p. 156.
[27] S. Goriely and E. Khan, Nucl. Phys. **A706**, 217 (2002).
[28] G. Audi and A. H. Wapstra, Nucl. Phys. **A595**, 409 (1995).
[29] S. Goriely, F. Tondeur, and J. M. Pearson, At. Data Nucl. Data Tables **77**, 311 (2001).
[30] P. Demetriou, C. Grama, and S. Goriely, Nucl. Phys. **A707**, 141 (2002).
[31] S. Goriely, Phys. Lett. B **436**, 10 (1998).
[32] J. Kopecky and R. E. Chrien, Nucl. Phys. **A468**, 285 (1987).
[33] Reference Input Parameter Library, IAEA-Tecdoc-1034, 1998, see also http://iaeand.iaea.or.at/ripl.
[34] A. Koning and J. P. Delaroche, Nucl. Phys. **A713**, 231 (2003).
[35] J. P. Jeukenne, A. Lejeune, and C. Mahaux, Phys. Rev. C **16**, 80 (1977).
[36] E. Bauge, J. P. Delaroche, and M. Girod, Phys. Rev. C **63**, 024607 (2001).
[37] F.-K. Thielemann, M. Arnould, and J. W. Truran, in *Advances in Nuclear Astrophysics*, edited by E. Vangioni-Flam, J. Audouze, M. Cassé, J.-P. Chieze, and J. Tran Thanh Van (Editions Frontières, Gif-sur-Yvette, 1986), p. 525.
[38] P. Demetriou and S. Goriely, Nucl. Phys. **A695**, 95 (2001).